Radiative coupling and decay dynamics of two two-level quantum emitters in arbitrary dielectric nanostructures

Gengyan Chen,[1] Jing-Feng Liu,[2,*] Renming Liu,[3] Guanghui Liu,[1] Yongzhu Chen,[1]
Zhanxu Chen,[1] and Xue-Hua Wang[3,†]

[1]*School of Optoelectronic Engineering, Guangdong Polytechnic Normal University, Guangzhou 510665, China*
[2]*College of Electronic Engineering, South China Agricultural University, Guangzhou 510642, China*
[3]*State Key Laboratory of Optoelectronic Materials and Technologies, School of Physics, Sun Yat-sen University, Guangzhou 510275, China*

Photon-mediated coherent interaction determines the decay dynamics of quantum emitters and facilitates on-chip quantum manipulation for quantum information processing. We derive a general formalism to efficiently and flexibly simulate the radiative coupling between two two-level quantum emitters in arbitrary dielectric nanostructures, based on which, the decay dynamics of the two quantum emitters can be obtained. We demonstrate this formalism to investigate the two quantum dots embedded in the photonic crystal L3 cavity. The anticrossing behavior in the evolution spectrum and the vacuum Rabi oscillation in the populations of the two quantum dots can be simulated in both zero and small dot-dot detuning case. Our formalism can serve as a flexible and efficient theoretical tool and may be further developed to handle the cases for different initial states, multiple quantum emitters, and arbitrary metallic nanostructures.

I. INTRODUCTION

On-demand coherent interaction between each arbitrarily chosen pair of two-level quantum emitters is essential ingredient for controlled gate operations in quantum information processing [1,2]. The quantum emitters, e.g., atoms, ions, superconducting qubits, quantum dots and color centers, are usually spatially localized and distantly separated to allow selective excitation, control, and read-out [3]. Consequently, the separated quantum emitters need to be connected via a quantum bus or, in a more general picture, quantum network [4]. In solid-state implementation, although the quantum dots can be coupled via the wave-function overlap and/or electrostatic dipole-dipole interaction (Förster resonant energy transfer, FRET), the effective coupling distance is only several nanometers [5,6]. As for long-distance interaction, the most natural choice of the quantum bus is photons, owing to the low decoherence rate, high velocity and matured on-chip photonic technology [2]. The photon emitted by an excited quantum emitter can be absorbed by the other unexcited one and the exchange of photons can induce the radiative coupling between the two quantum emitters [7].

The radiative coupling between two quantum emitters can be tailored by suitably designing the electromagnetic environment [8]. For instance, optical lenses [9] and waveguides [10–14] can collect and transfer the emitted photon from one quantum emitter to the other. More importantly, optical cavities [15] with spectrally peaked density of optical states and spatially concentrated electric field can enhance the photon-mediated interaction. The strong coupling of two quantum dots to the same cavity mode can be detected in small optical cavities [16–19] and the coherent nature was demonstrated [20]. The radiative coupling among few emitters in the single-mode cavity may form nanolaser beyond the limitations of conventional laser models for independently acting quantum emitters [21–23]. The strong coupling and entanglement of two quantum emitters can occur over longer distance in the photonic crystal (PC) dimers [24–26] and the hybrid plasmonic cavities [3].

Due to the radiative coupling, the decay dynamics of an ensemble of quantum emitters interacting with photonic modes differ from independent quantum emitters, and also strongly depend on the initial state and entanglement. When the initial excitations are distributed symmetrically/antisymmetrically among the indistinguishable and entangled quantum emitters, the collective state (Dicke state) is superradiant/subradiant [27–29], corresponding to an enhanced / suppressed interaction with the photonic modes. By adjusting the phase of the quantum emitters, the system can be tuned from subradiance to superradiance [30], the light field can be tuned from antibunched to (super-)bunched as well as nonclassical to classical behavior [31,32]. Furthermore, the radiation of two atoms in a single-mode cavity coherently [33] or off-resonantly [34] driven by an external field can considerably exceed the free-space superradiant behavior and result in hyperradiance. On the contrary, when the emitter-cavity coupling is much stronger than cavity dissipation rate and few particular quantum emitters are initially excited, i.e., the initial state contains no entanglement, the radiation trapping effect [35] appears, since the unexcited quantum emitters in the ensemble block the radiative relaxation of the excited ones to the cavity, elongate emission time, and reduce the photon number in the cavity [36]. Furthermore, the superradiance and radiation trapping can coexist

in the crossover regime of a moderately bad single-mode cavity [37].

The radiative coupling in simple electromagnetic environments can be efficiently simulated by the mode-expansion method [2,38] and the Green-function method [10,14,39,40]. However, as for complex electromagnetic environments, it is rather complicated to either find the complete eigenmodes or obtain the exact analytic Green function, which hinders the feasibility of these two methods. Previously, we have proposed a general classical approach [41] based on the Finite-Difference Time-Domain (FDTD) method [42] to simulate the transfer rate $\Gamma_{ij}(\omega)$ and collective level shift $\Delta_{ij}(\omega)$ [43] of the radiative coupling between ith and jth quantum emitters in arbitrary dielectric nanostructure. This approach requires two simulation runs: it first simulates $\Gamma_{ij}(\omega)$ via radiation power of dipoles, then calculates $\Delta_{ij}(\omega)$ by principal-value integration $\Delta_{ij}(\omega) = \frac{1}{2\pi}\mathcal{P}\int_0^{+\infty} d\omega' \frac{\Gamma_{ij}(\omega')}{\omega - \omega'}$. However, the calculation efficiency of this approach needs to be further improved. Besides, the decay dynamics of the quantum emitters in arbitrary dielectric nanostructures still remain a challenge, which is the main focus of this work.

In this paper, we propose a new formalism to efficiently and flexibly simulate the radiative coupling between two two-level quantum emitters in arbitrary dielectric nanostructures. More importantly, based on the radiative coupling, we propose an approach to calculate the decay dynamics of these two quantum emitters. As an illustrating application, we investigate the prototypical case of two quantum dots embedded in the PC L3 cavity [44]. The local coupling strength and level shift can be reproduced. The anti-crossing behavior among three polariton branches in the evolution spectrum can be simulated for both zero and small dot-dot detuning case. Besides, the vacuum Rabi oscillation in the populations of the two quantum dots can be observed, although approaching different steady values at the long-time limit for zero and small dot-dot detuning cases. Our formalism may serve as a flexible and efficient theoretical tool for the on-chip quantum manipulation in quantum information processing and may be further developed to handle the cases for different initial states, multiple quantum emitters, and arbitrary metallic nanostructures.

II. THEORY AND METHOD

In this section, we adopt quantum electrodynamics approach to investigate the radiative coupling and decay dynamics of two two-level quantum emitters (denoted as A and B) inside nonmagnetic, nondispersive, and lossless dielectric nanostructure. By adopting dipole approximation and rotating-wave approximation, the Hamiltonian of the system can be expressed as [45,46]

$$\hat{H} = \hbar \sum_{i=A,B} \omega_i |e_i\rangle\langle e_i| + \hbar \sum_{\lambda} \omega_{\lambda} \hat{a}_{\lambda}^{\dagger}\hat{a}_{\lambda}$$
$$+ \hbar \sum_{i=A,B} \sum_{\lambda} [g_{i\lambda}(\mathbf{r}_i)|g_i\rangle\langle e_i|\hat{a}_{\lambda}^{\dagger} + g_{i\lambda}^*(\mathbf{r}_i)|e_i\rangle\langle g_i|\hat{a}_{\lambda}]. \quad (1)$$

Here, ω_i is the transition frequency between the excited state $|e_i\rangle$ and the ground state $|g_i\rangle$ of the ith quantum emitter. ω_{λ}, $\hat{a}_{\lambda}$, and $\hat{a}_{\lambda}^{\dagger}$ are the eigenfrequency, annihilation operator and creation operator of the λth eigenmode of the dielectric

nanostructure, respectively. The coupling coefficient is

$$g_{i\lambda}(\mathbf{r}_i) = i\omega_i(2\varepsilon_0\hbar\omega_{\lambda})^{-1/2}u_i\hat{\mathbf{d}}_i \cdot \mathbf{E}_{\lambda}(\mathbf{r}_i). \quad (2)$$

Here, u_i and $\hat{\mathbf{d}}_i$ is the magnitude and direction of the transition dipole moment of the ith quantum emitter located at $\mathbf{r}_i$. $\mathbf{E}_{\lambda}(\mathbf{r})$ is the electric field of the λth eigenmode of the dielectric nanostructure.

We denote the system states as $|a\rangle = |e_A, g_B, 0\rangle$, $|b\rangle = |g_A, e_B, 0\rangle$, and $|c_{\lambda}\rangle = |g_A, g_B, 1_{\lambda}\rangle$, with only one excitation at quantum emitter A, B or the λth eigenmode of the dielectric nanostructure, respectively. We suppose that the initial state of the system is $|\psi(0)\rangle = |a\rangle$. The state of the system evolves as

$$|\psi(t)\rangle = a(t)|a\rangle + b(t)|b\rangle + \sum_{\lambda} c_{\lambda}(t)|c_{\lambda}\rangle = \hat{U}(t)|a\rangle. \quad (3)$$

Obviously, the probability amplitudes of the system states are the matrix elements of the evolution operator $\hat{U}(t)$, e.g., $a(t) = \langle a|\hat{U}(t)|a\rangle$ and $b(t) = \langle b|\hat{U}(t)|a\rangle$. The evolution operator can be calculated by [47]

$$\hat{U}(t) = \frac{1}{2\pi i}\int_{-\infty}^{+\infty} d\omega e^{-i\omega t}[\hat{G}^-(\omega) - \hat{G}^+(\omega)]. \quad (4)$$

Here, the evolution spectrum $\hat{G}^{\pm}(\omega) = \lim_{\eta \to 0^+} \hat{G}(z = \omega \pm i\eta)$ is the limit of the resolvent operator defined as

$$\hat{G}(z) = \frac{1}{z - \frac{\hat{H}}{\hbar}}. \quad (5)$$

As derived in Appendix A, the matrix elements of resolvent operator $\hat{G}(z)$ are

$$G_{ba}(z) = \langle b|\hat{G}(z)|a\rangle = \frac{W_{BA}(z)}{\Xi(z)}, \quad (6)$$

$$G_{aa}(z) = \langle a|\hat{G}(z)|a\rangle = \frac{z - \omega_B - W_{BB}(z)}{\Xi(z)}. \quad (7)$$

Here, we define $\Xi(z) = [z - \omega_A - W_{AA}(z)][z - \omega_B - W_{BB}(z)] - W_{AB}(z)W_{BA}(z)$. The coupling matrix element is

$$W_{ij}(z) = \sum_{\lambda} \frac{g_{i\lambda}^*(\mathbf{r}_i)g_{j\lambda}(\mathbf{r}_j)}{z - \omega_{\lambda}}, i, j = A, B. \quad (8)$$

Obviously, the key to investigate the decay dynamics is the calculation of the coupling matrix element $W_{ij}^{\pm}(\omega) = \lim_{\eta \to 0^+} W_{ij}(z = \omega \pm i\eta)$. According to Eq. (2), we may obtain

$$W_{ij}^{\pm}(\omega) = \sum_{\lambda} \frac{u_i^* u_j \omega_i \omega_j}{2\varepsilon_0\hbar\omega_{\lambda}}[\hat{\mathbf{d}}_i \cdot \mathbf{E}_{\lambda}^*(\mathbf{r}_i)][\hat{\mathbf{d}}_j \cdot \mathbf{E}_{\lambda}(\mathbf{r}_j)]$$
$$\times [\mathcal{P}\frac{1}{\omega - \omega_{\lambda}} \mp i\pi\delta(\omega - \omega_{\lambda})]. \quad (9)$$

Here, $\mathcal{P}$ denote the principal value. Obviously, $W_{ij}^+(\omega)$ is the complex conjugate of $W_{ij}^-(\omega)$. When $i \neq j$, $W_{ij}^{\pm}(\omega) = \Delta_{ij}(\omega) \mp \frac{i}{2}\Gamma_{ij}(\omega)$ characterizes the radiative coupling between the ith and the jth quantum emitter mediated by the eigenmodes of the dielectric nanostructure, whose imaginary and real part is related to the transfer rate $\Gamma_{ij}(\omega)$ and collective level shift $\Delta_{ij}(\omega)$, respectively [41,43]. When $i = j$, $W_{ii}^{\pm}(\omega) = \Delta_{ii}(\mathbf{r}_i, \omega) \mp \frac{i}{2}\Gamma_{ii}(\mathbf{r}_i, \omega)$ characterizes the local coupling between the ith quantum emitter and the eigenmodes

of the dielectric nanostructure. The real part of $W_{ii}^{\pm}(\omega)$ is the level shift $\Delta_{ii}(\mathbf{r}_i, \omega) = \frac{1}{2\pi} \mathcal{P} \int_0^{+\infty} d\omega' \frac{\Gamma_{ii}(\mathbf{r}_i, \omega')}{\omega - \omega'}$ while the absolute value of the imaginary part of $W_{ii}^{\pm}(\omega)$ is half of the local coupling strength $\Gamma_{ii}(\mathbf{r}_i, \omega) = 2\pi \sum_{\lambda} |g_{i\lambda}(\mathbf{r}_i)|^2 \delta(\omega - \omega_\lambda)$ [48].

The coupling matrix element $W_{ij}^{-}(\omega)$ can be calculated as

$$W_{ij}^{-}(\omega) = -\frac{u_i^* u_j \omega_i}{\hbar d_j^*(\omega)\omega} \hat{\mathbf{d}}_i \cdot \mathbf{E}_j^*(\mathbf{r}_i, \omega). \tag{10}$$

The detailed derivation can be found in Appendix B. Obviously, $W_{ij}^{-}(\omega)$ ($i, j = A, B$) can be calculated based on the complex amplitude of the electric field $\mathbf{E}_j(\mathbf{r}_i, \omega)$, which is excited by the jth dipole [with complex amplitude $d_j(\omega)$] and detected at the location $\mathbf{r}_i$ of the ith dipole. $\mathbf{E}_j(\mathbf{r}_i, \omega)$ can be simulated directly in frequency domain by, e.g., the COMSOL Multiphysics. Alternatively, we can first simulate $\mathbf{E}_j(\mathbf{r}_i, t)$ in time domain by, e.g., the FDTD method, and then obtain $\mathbf{E}_j(\mathbf{r}_i, \omega)$ by Fourier transform or Padé approximation with Baker's algorithm [49]. The accuracy of this formalism is mainly limited by the accuracy of the numerical methods for simulating $\mathbf{E}_j(\mathbf{r}_i, \omega)$. As for the efficiency, the Padé approximation is extremely efficient for the nanostructures with highly localized field distribution, such as nanocavities. Our test for the PC L3 cavity shows the Padé approximation can save computation time by about 200 times comparing with the Fourier transform [48]. Besides, the coupling matrix elements $W_{ij}^{\pm}(\omega)$ including the transfer rate $\Gamma_{ij}(\omega)$ and collective level shift $\Delta_{ij}(\omega)$ can be simultaneously calculated in a single simulation run, without principal-value integration $\Delta_{ij}(\omega) = \frac{1}{2\pi} \mathcal{P} \int_0^{+\infty} d\omega' \frac{\Gamma_{ij}(\omega')}{\omega - \omega'}$, which is much more efficient than the previous approach [41].

Conventionally, the local coupling between a single quantum emitter and a cavity mode can be characterized by the Purcell factor $F_P = \frac{3}{4\pi^2} (\frac{\lambda}{n})^3 \frac{Q}{V_m}$ [50] or coupling coefficient $g = u\sqrt{\frac{\hbar\omega}{2\varepsilon_0 V_m}}$ [51]. These two approaches both assumes a perfect spectral, spatial, and polarization matching, and requires the effective mode volume $V_m = \frac{\int_V \varepsilon_r(\mathbf{r})|\mathbf{E}_c(\mathbf{r})|^2 d\mathbf{r}}{\max[\varepsilon_r(\mathbf{r})|\mathbf{E}_c(\mathbf{r})|^2]}$. To calculate V_m, the electric field distribution $\mathbf{E}_c(\mathbf{r})$ in the whole space (mainly inside and near the cavity) should be simulated and then integrated, which consumes massive computational time and memory. In contrast, our formalism can calculate the radiative coupling between two quantum emitters at any location, along any polarization direction, with any transition frequency, inside arbitrary dielectric nanostructures. Besides, only the electric fields at the two quantum emitters (rather than those of the whole space) need to be simulated, which saves massive computational time and memory.

As for the near-field coupling in small optical cavities, the coupling matrix elements $W_{ij}^{\pm}(\omega)$ of Eq. (8) sum up the coupling coefficients $g_{i\lambda}(\mathbf{r}_i)$ between each quantum emitter (with transition dipole moment $u_i \hat{\mathbf{d}}_i$) and all the eigenmodes $\mathbf{E}_\lambda(\mathbf{r}_i)$ of the dielectric nanostructure, and can be exactly calculated via the complex amplitudes of the electric field $\mathbf{E}_j(\mathbf{r}_i, \omega)$. Since the $\mathbf{E}_j(\mathbf{r}_i, \omega)$ including the near field can be exactly simulated by either the COMSOL Multiphysics or the FDTD method, the near-field coupling mediated by

any eigenmode of the small optical cavities is taken into consideration by our formalism.

Nevertheless, for simplicity, in the Hamiltonian of Eq. (1), we ignore the direct interaction (not mediated by any photon) between the two quantum emitters, i.e., the electrostatic dipole-dipole interaction (FRET). FRET is the nonradiative energy transfer mediated by a (quantum-mechanical) coupling between the transition dipoles of the donor and acceptor quantum emitter described by a (point)-dipole-dipole interaction [52]. The FRET rate is dependent on the inverse sixth power of the inter-emitter separation, so the effective coupling distance is typically only several nanometers. Obviously, in small optical cavities, when the interdot separation is comparable to a visible wavelength, the FRET is negligible.

III. RESULT AND DISCUSSION

To demonstrate and verify our formalism, we apply it to the prototypical case of two quantum dots embedded in the PC L3 cavity reported in Ref. [2], as shown in Fig. 1. The GaAs PC slab suspended in air has a triangular lattice of circular air holes. The refractive index of GaAs is $n = 3.41$. The lattice constant is $a = 260$ nm. The slab thickness is 120 nm. The air hole radii are $r = 65$ nm. The PC L3 cavity is made by missing three air holes in a line. The two air holes at both cavity edges are shifted outwards by $0.15a$ and their radii are decreased to $0.8r$ in order to increase its quality (Q) factor [44].

The $E_y(\mathbf{r})$ and $E_x(\mathbf{r})$ components of the electric field $\mathbf{E}_c(\mathbf{r})$ of the fundamental cavity mode [53] are simulated by FDTD method and shown in Fig. 1. This spatial distribution is typical among similar PC L3 cavities [54–56]. Most electromagnetic energy of the cavity mode is localized inside the three missed air holes due to the two-dimensional photonic bandgap and is also confined inside the slab by the total internal reflection [57].

For this high-Q leaky optical cavity, the divergence of the cavity modes at large distances is slow and not discernible in practical calculations due to limited numerical accuracy [58], as validated in Fig. 1. The simulation domain for the PC L3 cavity is $25a$, $22a$, and $10a$ along x, y, and z direction, respectively, which is large enough to obtain convergent results according to our convergence test. Besides, our formalism simulates the radiative coupling between two quantum emitters via the electric fields at the two quantum emitters, without the calculation of the effective mode volume.

The two quantum dots (denoted as A and B) are embedded at the secondary maxima of the $E_y(\mathbf{r})$ component and oriented along y direction, so the interactions between the cavity mode and each quantum dot can both reach maxima. The spontaneous emission lifetimes of the two quantum dots in GaAs without PC pattern are both 1 ns.

We assume that at $t = 0$, quantum dot A and B are in excited and ground state, respectively, and the PC L3 cavity has no photon, i.e., the initial state of the system is $|\psi(0)\rangle = |a\rangle = |e_A, g_B, 0\rangle$. The two quantum dots are in phase. We start from the zero dot-dot and dot-cavity detuning case $\omega_A = \omega_B = \omega_c$. To investigate the decay dynamics of the two quantum dots inside the PC L3 cavity, we need to calculate the coupling matrix elements $W_{ij}^{\pm}(\omega)(i, j = A, B)$, whose keys
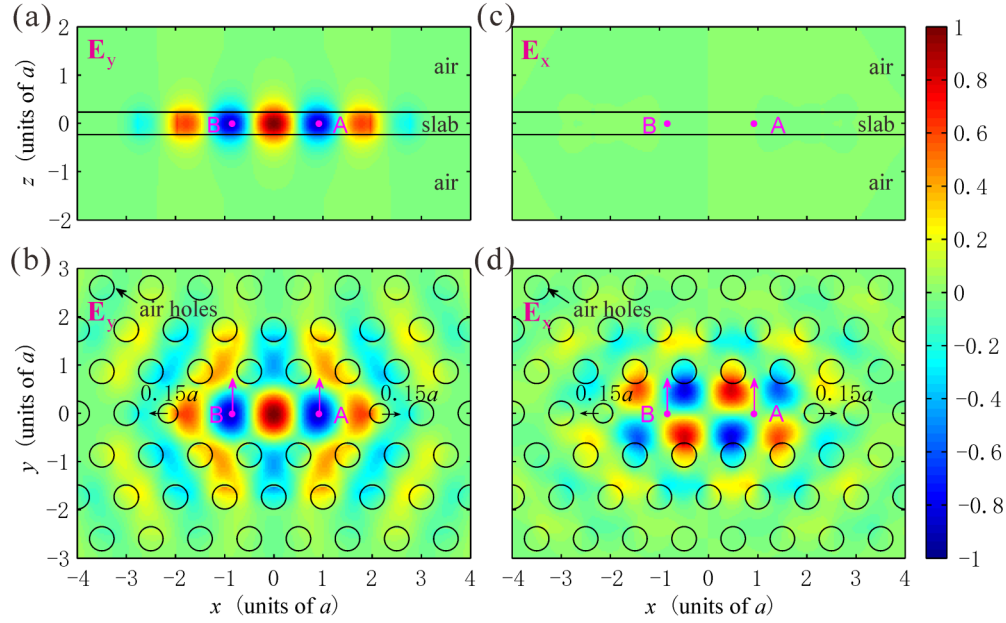
FIG. 1. Two quantum dots embedded in the PC L3 cavity. (a, b) $E_y(\mathbf{r})$ and (c, d) $E_x(\mathbf{r})$ component of the normalized electric field $\mathbf{E}_c(\mathbf{r})$ of the PC L3 cavity mode on (a, c) $y = 0$ and (b, d) $z = 0$ plane, respectively. The resonant frequency of the cavity is $\hbar\omega_c = 1306.11$ meV. The two horizontal black lines in (a, c) denote the top and bottom surfaces of the slab. The black circles in (b, d) denote the air holes. The axes adopt the unit of lattice constant a. The magenta dots denote the locations $\mathbf{r}_A = (0.85a, 0, 0)$ and $\mathbf{r}_B = (-0.85a, 0, 0)$ of the two quantum dots. The magenta arrows denote their directions $\hat{\mathbf{d}}_A$ and $\hat{\mathbf{d}}_B$.

are $\mathbf{E}_j(\mathbf{r}_i, \omega)$. As shown in Fig. 1, since both the geometry and cavity mode are symmetric at $\mathbf{r}_A$ and $\mathbf{r}_B$, the four $\mathbf{E}_j(\mathbf{r}_i, \omega)$ are exactly the same. Consequently, based on Eq. (10), the four $W_{ij}^-(\omega)$ in this case are also identical, as shown in Fig. 2(a). The four $W_{ij}^+(\omega)$ are the complex conjugates of the four $W_{ij}^-(\omega)$, respectively, according to Eq. (9).

Based on the calculated $W_{ij}^-(\omega)$, we can compare the relative strengths between the FRET and the radiative coupling. As examples, the FRET rate is estimated to be $(38 \, \text{ps})^{-1}$ for the CdSe/ZnS quantum dots with interdot separation of 5.4 nm [59], and $(120 \, \text{ps})^{-1}$ for the InP quantum dots

with interdot separation of 7 nm [5]. The interdot separation between the two quantum dots inside the PC L3 cavity is $1.7a = 442$ nm. At this interdot separation, according to the dependence of the inverse sixth power, the FRET rate is estimated to be $(11.4 \, \text{s})^{-1}$ for the CdSe/ZnS quantum dots, and $(7.6 \, \text{s})^{-1}$ for the InP quantum dots, which are both about 12 orders of magnitude smaller than the peak value (at resonance) $\frac{1.76 \, \text{meV}}{\hbar} = (2.35 \, \text{ps})^{-1}$ of the imaginary part of $W_{ij}(\omega)$. Obviously, in small optical cavities, when the interdot separation is comparable to a visible wavelength, the radiative coupling dominates over the FRET, which validates the conclusion made at the end of Sec. II.
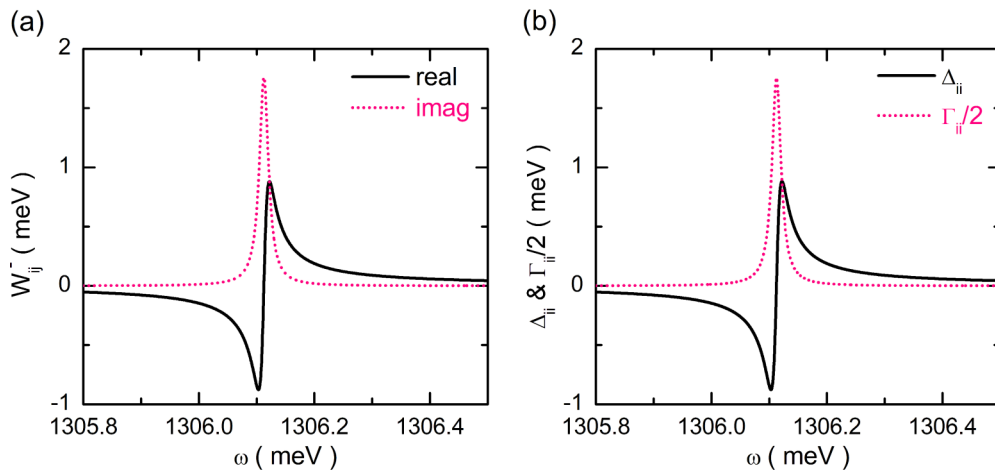

FIG. 2. Radiative coupling between two quantum dots in the PC L3 cavity for the zero dot-dot and dot-cavity detuning case $\omega_A = \omega_B = \omega_c$. (a) Coupling matrix elements $W_{ij}^-(\omega)$ ($i, j = A, B$). The solid black and dotted pink lines are the real and imaginary parts, respectively. (b) Level shift $\Delta_{ii}(\mathbf{r}_i, \omega)$ and half of the local coupling strength $\Gamma_{ii}(\mathbf{r}_i, \omega)$ for each quantum dot $i = A, B$.
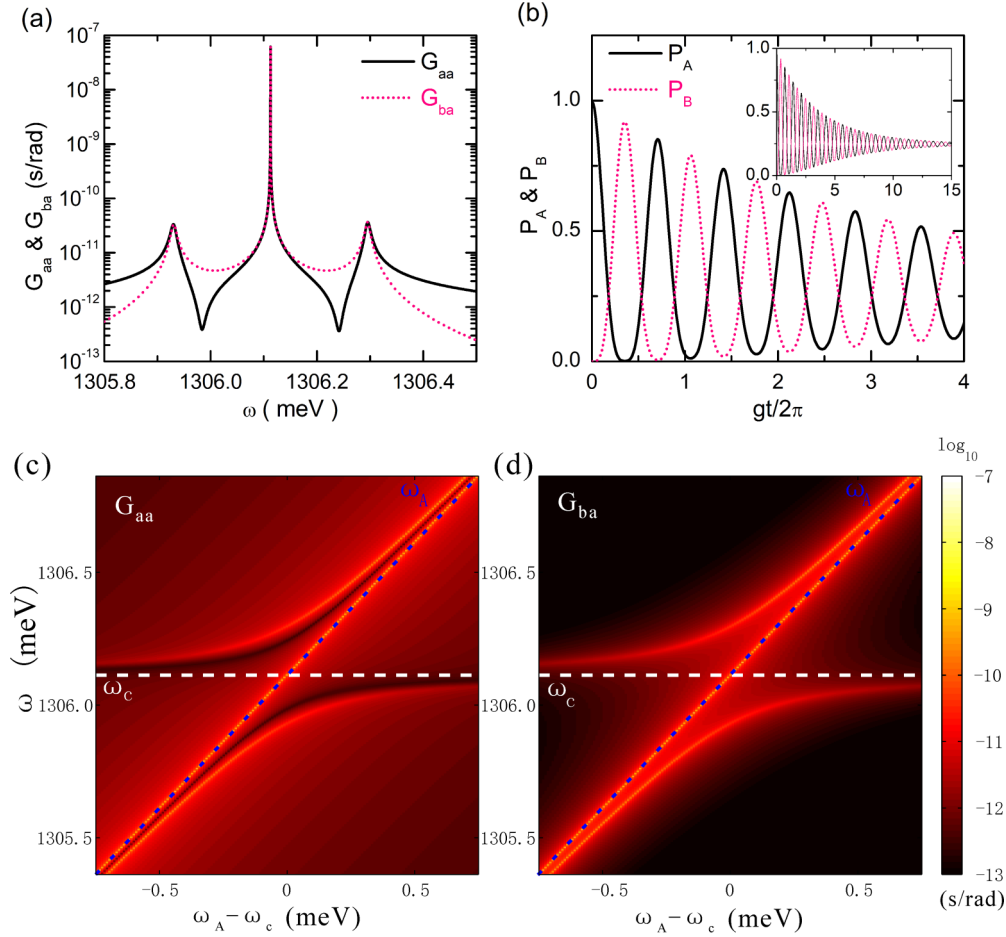
FIG. 3. Decay dynamics of the two quantum dots in the PC L3 cavity with zero dot-dot detuning $\omega_A = \omega_B$. (a) Modulus of the evolution spectrum $G_{aa}^{\pm}(\omega)$ and $G_{ba}^{\pm}(\omega)$ for zero dot-cavity detuning $\omega_A = \omega_c$. (b) Population $P_A(t)$ and $P_B(t)$ for zero dot-cavity detuning $\omega_A = \omega_c$. Inset: population for longer time. (c, d) Modulus of the evolution spectrum (c) $G_{aa}^{\pm}(\omega)$ and (d) $G_{ba}^{\pm}(\omega)$ for different dot-cavity detunings $\omega_A - \omega_c$. The dashed white line denotes ω_c. The dotted blue line denotes ω_A (ω_B).

When $i = j$, $W_{ii}^{\pm}(\omega)$ characterizes the local coupling between the ith quantum dot and the eigenmodes of the dielectric nanostructure. We adopt our previous method proposed in Refs. [48,60] to simulate the local coupling strength $\Gamma_{ii}(\mathbf{r}_i, \omega)$. Then, based on the local coupling strength, the level shift is calculated via the principal-value integral as $\Delta_{ii}(\mathbf{r}_i, \omega) = \frac{1}{2\pi} \mathcal{P} \int_0^{+\infty} d\omega' \frac{\Gamma_{ii}(\mathbf{r}_i, \omega')}{\omega - \omega'}$. Since both the geometry and cavity mode are symmetric at $\mathbf{r}_A$ and $\mathbf{r}_B$, the results for quantum dot A and B are identical, as shown in Fig. 2(b). Comparing Fig. 2(a) with Fig. 2(b), we can confirm that the real part of $W_{ii}^{\pm}(\omega)$ is the level shift $\Delta_{ii}(\mathbf{r}_i, \omega)$ while the absolute value of the imaginary part of $W_{ii}^{\pm}(\omega)$ is half of the local coupling strength $\Gamma_{ii}(\mathbf{r}_i, \omega)$. We can adopt the formalism proposed in this paper to directly, without performing principal-value integral, obtain $\Gamma_{ii}(\mathbf{r}_i, \omega)$ and $\Delta_{ii}(\mathbf{r}_i, \omega)$ from the imaginary and real part, respectively, of the calculated $W_{ij}^{-}(\omega)$. Based on $\Gamma_{ii}(\mathbf{r}_i, \omega)$ and $\Delta_{ii}(\mathbf{r}_i, \omega)$, the decay dynamics of single two-level quantum emitter in arbitrary dielectric nanostructure can be further investigated [48,60].

Based on the local coupling strength $\Gamma_{ii}(\mathbf{r}_i, \omega)$, by our previous method [48], we can obtain the Q factor of the PC L3 cavity $Q = 68891$ and the modulus of coupling coefficient

$\hbar|g_{ic}(\mathbf{r}_i)| = 0.129$ meV. The calculated $\hbar|g_{ic}(\mathbf{r}_i)|$ is slightly different from 0.125 meV given in Ref. [2] since the location $\mathbf{r}_i$ of the ith quantum dot might be slightly different, which is not explicitly given in Ref. [2].

Based on the coupling matrix elements $W_{ij}^{\pm}(\omega)$, by Eqs. (6) and (7), we can calculate the evolution spectrum $G_{aa}^{\pm}(\omega)$ and $G_{ba}^{\pm}(\omega)$. Obviously, $G_{aa}^{+}(\omega)$ and $G_{ba}^{+}(\omega)$ are the complex conjugates of $G_{aa}^{-}(\omega)$ and $G_{ba}^{-}(\omega)$, respectively. Figure 3(a) shows that the modulus of $G_{aa}^{\pm}(\omega)$ and $G_{ba}^{\pm}(\omega)$ both have three peaks. The central peak at ω_A (ω_B) is the dark mode, i.e., the antisymmetric state of the two quantum dots. The central peak is extremely narrow since the linewidths of the two quantum dots are negligible. On the contrary, the two side peaks symmetrically beside ω_A (ω_B) are the bright modes composed of the symmetric state of the two quantum dots and the cavity mode. The two side peaks are relatively wide since the linewidth of the cavity mode $\kappa = \omega_c/Q$ is relatively large. The vacuum Rabi splitting between the upper and lower polaritons is $\hbar\Omega = 0.366$ meV $= 2\sqrt{2}\hbar|g_{ic}(\mathbf{r}_i)|$. In other words, the two quantum dots with symmetric state behaves as a single exciton with an effective modulus of coupling coefficient of $\sqrt{2}|g_{ic}(\mathbf{r}_i)|$ [2].

The time-dependent radiative excitation transfer is a useful coupling mechanism between different qubits in a semiconductor-based quantum gate architecture [2]. The time-dependent probabilities of excitation, i.e., the population of quantum dot A and B as $P_A(t) = |a(t)|^2$ and $P_B(t) = |b(t)|^2$ can be calculated by Eq. (4), based on the evolution spectrum $G_{aa}^{\pm}(\omega)$ and $G_{ba}^{\pm}(\omega)$. As shown in Fig. 3(b), initially, quantum dot A is in excited state while quantum dot B is in ground state. Due to the radiative coupling between the two quantum dots mediated by the cavity mode, the populations of the two quantum dots both oscillate at the frequency of $\Omega/2 = \sqrt{2}|g_{ic}(\mathbf{r}_i)|$. Due to the cavity leakage $\kappa = \omega_c/Q$, the amplitudes of the two oscillating populations decay at the rate of $2\omega_c/Q$. Due to the dark state and negligible nonradiative decay mechanism of the quantum dots, the two populations both eventually approach the steady value of 0.25, as shown in the inset of Fig. 3(b). As we mentioned in the Introduction, this radiation trapping effect originates from the absence of indistinguishability and entanglement in the initial state of the two quantum dots.

We now proceed to vary the transition frequencies of both quantum dots while keeping zero dot-dot detuning $\omega_A = \omega_B$, and calculate the evolution spectrum $G_{aa}^{\pm}(\omega)$ and $G_{ba}^{\pm}(\omega)$ for different dot-cavity detunings $\omega_A - \omega_c$. As shown in Figs. 3(c) and 3(d), for each detuning $\omega_A - \omega_c$, the evolution spectrum $G_{aa}^{\pm}(\omega)$ and $G_{ba}^{\pm}(\omega)$ both have three peaks. The central peak at ω_A (ω_B) is the dark mode, i.e., the antisymmetric state of the two quantum dots. For large dot-cavity detuning $|\omega_A - \omega_c|$, one side peak approaches ω_A (ω_B) (contributed mainly from the transition of the quantum dots) and the other side peak approaches ω_c (contributed mainly from the resonance of the cavity). As dot-cavity detuning $|\omega_A - \omega_c|$ decreases, the two side peaks gradually repel each other (both contributed from the two quantum dots and the cavity), which is similar to the anti-crossing behavior in the strong-coupling system composed of only a single quantum dot and the PC L3 cavity [60]. For zero dot-cavity detuning, the two side peaks locate symmetrically at both side of ω_c and form two polaritonic states, which is the case of Fig. 3(a). In experiment, the exact resonance between the cavity mode and the quantum dots can be tuned by various techniques. The transition frequency of the quantum dot can be tuned by temperature [61–64] or operando strain [65], while the resonant frequency of the PC cavity can be tuned by thin-film condensation [66] or digital etching [67].

In experiment, due to the inhomogeneous distribution of the shape and size, the transition frequencies of the quantum dots are detuned, which may influence the radiative coupling and decay dynamics of the quantum dots. We now turn to investigate this realistic case and assume the small dot-dot detuning as $\hbar(\omega_A - \omega_B) = 0.3$ meV. First, we consider the zero dot-cavity detuning case $(\omega_A + \omega_B)/2 = \omega_c$. The evolution spectrum $G_{aa}^{\pm}(\omega)$ and $G_{ba}^{\pm}(\omega)$, as shown in Fig. 4(a), both have three peaks. Comparing with the zero dot-dot detuning case in Fig. 3(a), the central peak at ω_c is much lower and wider since the central peak is contributed from not only the two quantum dots, but also the cavity. So, the central peak is no longer a dark state. Besides, the vacuum Rabi splitting Ω between the two side peaks is wider due to the additional dot-dot detuning.

Comparing with the zero dot-dot detuning case in Fig. 3(b), the population $P_A(t)$ and $P_B(t)$ of the two quantum dots for

the small dot-dot detuning case in Fig. 4(b) both oscillate at a larger frequency $\Omega/2$. Since the three peaks are all contributed from the two quantum dots and the cavity, the three polaritons may all decay into vacuum via the leakage of the cavity $\kappa = \omega_c/Q$. Hence, the populations of the two quantum dots both eventually approach the steady value of 0, at the rate of $2\omega_c/Q$, as shown in the inset of Fig. 4(b).

We now vary the transition frequencies of both quantum dots while keeping dot-dot detuning as $\hbar(\omega_A - \omega_B) = 0.3$ meV, and calculate the evolution spectrum $G_{aa}^{\pm}(\omega)$ and $G_{ba}^{\pm}(\omega)$ for different dot-cavity detunings $(\omega_A + \omega_B)/2 - \omega_c$. As shown in Figs. 4(c) and 4(d), for each dot-cavity detuning $(\omega_A + \omega_B)/2 - \omega_c$, the evolution spectrum $G_{aa}^{\pm}(\omega)$ and $G_{ba}^{\pm}(\omega)$ both have three peaks. For large dot-cavity detuning $|(\omega_A + \omega_B)/2 - \omega_c|$, two peaks approach ω_A and ω_B (contributed mainly from the two quantum dots) and the third peak approaches ω_c (contributed mainly from the cavity). As dot-cavity detuning $|(\omega_A + \omega_B)/2 - \omega_c|$ decreases, the three peaks gradually repel each other and form three polaritonic states, all contributed from the two quantum dots and the cavity. For zero dot-cavity detuning, the central peak locates exactly at ω_c and the two side peaks locate symmetrically at both sides of ω_c, which is the case of Fig. 4(a).

The inhomogeneous distribution of the shape and size of quantum dots results in not only the transition frequency detuning, but also the lifetime mismatch, which influences the transition dipole moment, coupling coefficient and coupling matrix elements, subsequently. According to our further calculation, for lifetime mismatch of 1.44 times between quantum dot A and B, the anti-crossing behavior among the upper polariton, lower polariton and dark mode (or middle polariton) branches in the evolution spectrum of varying dot-cavity detuning for zero (or small) dot-dot detuning case can still be observed, however, with different vacuum Rabi splitting. For zero dot-dot detuning case, the population of quantum dot A and B both oscillate at a different frequency. However, for small dot-dot detuning case $\hbar(\omega_A - \omega_B) = 0.3$ meV, the population of quantum dot A and, especially, B no longer oscillate perfectly due to the coexistence of small transition frequency detuning and large lifetime mismatch (1.44 times). Obviously, the robustness of this system in experimental implementation needs further verification.

Although we simulate two quantum emitters in the PC L3 cavity as a demonstration, our formalism do not simulate the band structures of PCs, and can be applied to arbitrary dielectric nanostructures.

IV. CONCLUSION

We develop a formalism to efficiently calculate the radiative coupling and decay dynamics of two two-level quantum emitters in arbitrary dielectric nanostructures. The coupling matrix element $W_{ij}^{\pm}(\omega)$ can be calculated based on the complex amplitudes of the electric field $\mathbf{E}_j(\mathbf{r}_i, \omega)$, which is excited by the jth dipole and detected at the location of the ith dipole $\mathbf{r}_i$. Based on the coupling matrix element, the evolution spectrum and hence the decay dynamics of the two quantum emitters can be obtained. In the prototypical case of two quantum dots embedded in the PC L3 cavity, we apply our formalism to directly reproduce the local coupling strength
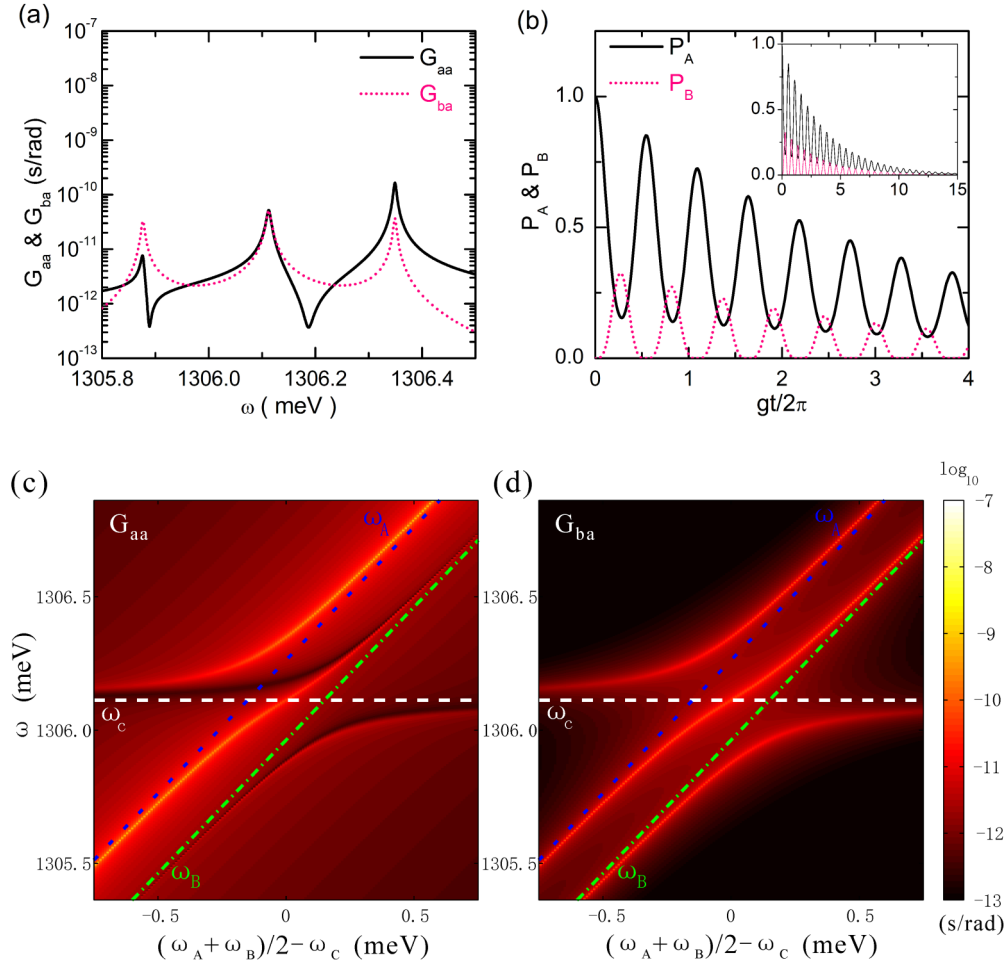
FIG. 4. Decay dynamics of the two quantum dots in the PC L3 cavity with small dot-dot detuning as $\hbar(\omega_A - \omega_B) = 0.3$ meV. (a) Modulus of the evolution spectrum $G_{aa}^{\pm}(\omega)$ and $G_{ba}^{\pm}(\omega)$ for zero dot-cavity detuning $(\omega_A + \omega_B)/2 = \omega_c$. (b) Population $P_A(t)$ and $P_B(t)$ for zero dot-cavity detuning $(\omega_A + \omega_B)/2 = \omega_c$. Inset: population for longer time. (c, d) Modulus of the evolution spectrum (c) $G_{aa}^{\pm}(\omega)$ and (d) $G_{ba}^{\pm}(\omega)$ for different dot-cavity detunings $(\omega_A + \omega_B)/2 - \omega_c$. The dashed white line denotes ω_c. The dotted blue line denotes ω_A. The dash-dotted green line denotes ω_B.

$\Gamma_{ii}(\mathbf{r}_i, \omega)$ and the level shift $\Delta_{ii}(\mathbf{r}_i, \omega)$. We can simulate the anti-crossing behavior among the upper polariton, lower polariton and dark mode (or middle polariton) branches in the evolution spectrum of varying dot-cavity detuning for zero (or small) dot-dot detuning case. The vacuum Rabi oscillation in the populations of the two quantum dots for both zero and small dot-dot detuning cases can be observed, although approaching different steady values at the long-time limit.

The present formalism can be applied to a large variety of photonic structures, such as PC slab [68] and dimers [24–26]. The doubly degenerated orthogonally polarized dipole modes of the PC H1 cavity [69] might enrich the radiative coupling and result in interesting decay dynamics of two quantum emitters. The bowtie PC cavities with ultrasmall mode volume below the diffraction limit [70,71] might be adopted to realize the strong radiative coupling if two quantum emitters are positioned exactly at the bowtie tips (hot spots of the cavity mode).

The formalism can be further developed to handle different initial states of the two quantum emitters with indistinguishability and entanglement, which can be boosted by cascaded cavities [72], and predict different dynamic behaviors and radiation characteristics. We can also develop the formalism to investigate the decay dynamics of more than two quantum emitters, which is essential for multiqubit manipulation. Most importantly, due to the abundant physical phenomena and promising application prospect in plasmonics [73–76], further efforts should be made to develop the formalism to simulate the radiative coupling and decay dynamics of two two-level quantum emitters in arbitrary metallic nanostructures.

ACKNOWLEDGMENT

APPENDIX A

The first two terms of Eq. (1) are the noninteraction Hamiltonian $\hat{H}_0$ and the last term is the interaction Hamiltonian $\hat{H}_I$. Equation (5) can be rewritten as

$$\left(z - \frac{\hat{H}_0}{\hbar}\right)\hat{G}(z) = 1 + \frac{\hat{H}_I}{\hbar}\hat{G}(z). \tag{A1}$$

Regarding the completeness relationship $I = |a\rangle\langle a| + |b\rangle\langle b| + \sum_\mu |c_\mu\rangle\langle c_\mu|$, the matrix element of both sides of Eq. (A1) between $\langle a|$ and $|a\rangle$ is

$$(z - \omega_A)G_{aa}(z) = 1 + \sum_\lambda g_{A\lambda}^*(\mathbf{r}_A)G_{\lambda a}(z). \tag{A2}$$

The matrix element between $\langle b|$ and $|a\rangle$ is

$$(z - \omega_B)G_{ba}(z) = \sum_\lambda g_{B\lambda}^*(\mathbf{r}_B)G_{\lambda a}(z). \tag{A3}$$

The matrix element between $\langle c_\lambda|$ and $|a\rangle$ is

$$(z - \omega_\lambda)G_{\lambda a}(z) = g_{A\lambda}(\mathbf{r}_A)G_{aa}(z) + g_{B\lambda}(\mathbf{r}_B)G_{ba}(z). \tag{A4}$$

Eliminating $G_{\lambda a}(z) = \langle c_\lambda|\hat{G}(z)|a\rangle$ in Eqs. (A2), (A3), and (A4), and adopting the coupling matrix element of Eq. (8), we can obtain

$$\begin{aligned} [z - \omega_A - W_{AA}(z)]G_{aa}(z) &= 1 + W_{AB}(z)G_{ba}(z), \\ [z - \omega_B - W_{BB}(z)]G_{ba}(z) &= W_{BA}(z)G_{aa}(z). \end{aligned} \tag{A5}$$

By solving Eq. (A5), we can obtain Eqs. (6) and (7) [41].

APPENDIX B

The two curl Maxwell equations in the nonmagnetic, nondispersive, and lossless dielectric nanostructure with dielectric constant $\varepsilon(\mathbf{r}) = \varepsilon_0\varepsilon_r(\mathbf{r})$ are

$$\nabla \times \mathbf{E}(\mathbf{r}, t) = -\frac{\partial \mu_0 \mathbf{H}(\mathbf{r}, t)}{\partial t}, \tag{B1}$$

$$\nabla \times \mathbf{H}(\mathbf{r}, t) = \mathbf{J}_\gamma(\mathbf{r}, t) + \frac{\partial \varepsilon(\mathbf{r})\mathbf{E}(\mathbf{r}, t)}{\partial t} + \frac{\partial \mathbf{P}(\mathbf{r}, t)}{\partial t}. \tag{B2}$$

Here, the electric field $\mathbf{E}(\mathbf{r}, t)$ and the magnetic field $\mathbf{H}(\mathbf{r}, t)$ are functions of both space $\mathbf{r}$ and time t. Following the approach in Ref. [77], for convenience of analysis, we introduce the dissipation current density $\mathbf{J}_\gamma(\mathbf{r}, t)$, assumed to be linear function of electric field as $\mathbf{J}_\gamma(\mathbf{r}, t) = \gamma\varepsilon(\mathbf{r})\mathbf{E}(\mathbf{r}, t)$. For lossless dielectric nanostructure, at the end of calculation, the magnitude of proportionality constant goes to zero: $\gamma \to 0^+$. Hence, this magnitude is of no real consequence. The dipole source (polarization density) $\mathbf{P}(\mathbf{r}, t)$ is equivalent to the current source (current density) $\mathbf{J}(\mathbf{r}, t)$ as $\mathbf{J}(\mathbf{r}, t) = \frac{\partial \mathbf{P}(\mathbf{r}, t)}{\partial t}$.

The electric field can be expanded in terms of a complete set of eigenmodes of the dielectric nanostructure as

$$\mathbf{E}(\mathbf{r}, t) = \sum_\lambda \alpha_\lambda(t)\mathbf{E}_\lambda(\mathbf{r}). \tag{B3}$$

These eigenmodes obey the eigenmode equation:

$$\frac{1}{\varepsilon_r(\mathbf{r})}\nabla \times [\nabla \times \mathbf{E}_\lambda(\mathbf{r})] = \frac{\omega_\lambda^2}{c^2}\mathbf{E}_\lambda(\mathbf{r}). \tag{B4}$$

These eigenmodes are orthonormal to each other as

$$\int_V \varepsilon_r(\mathbf{r})\mathbf{E}_\mu^*(\mathbf{r}) \cdot \mathbf{E}_\lambda(\mathbf{r})d\mathbf{r} = \delta_{\mu\lambda}. \tag{B5}$$

Taking curl of both side of Eq. (B1) and substituting Eq. (B2) into it, we can obtain

$$\nabla \times \nabla \times \mathbf{E}(\mathbf{r}, t) = -\mu_0\gamma\varepsilon(\mathbf{r})\frac{\partial}{\partial t}\mathbf{E}(\mathbf{r}, t) - \mu_0\varepsilon(\mathbf{r})\frac{\partial^2\mathbf{E}(\mathbf{r}, t)}{\partial t^2} - \mu_0\frac{\partial^2\mathbf{P}(\mathbf{r}, t)}{\partial t^2}. \tag{B6}$$

Substituting Eq. (B3) into Eq. (B6), and considering Eq. (B4), we can obtain

$$\sum_\lambda \left[\omega_\lambda^2\alpha_\lambda(t) + \gamma\dot{\alpha}_\lambda(t) + \ddot{\alpha}_\lambda(t)\right]\varepsilon_r(\mathbf{r})\mathbf{E}_\lambda(\mathbf{r}) = -\frac{1}{\varepsilon_0}\frac{\partial^2\mathbf{P}(\mathbf{r}, t)}{\partial t^2}. \tag{B7}$$

Taking dot product of both side of Eq. (B7) by $\mathbf{E}_\mu^*(\mathbf{r})$, integrating over the whole space and considering Eq. (B5), we can obtain

$$\omega_\lambda^2\alpha_\lambda(t) + \gamma\dot{\alpha}_\lambda(t) + \ddot{\alpha}_\lambda(t) = -\frac{1}{\varepsilon_0}\int_V \mathbf{E}_\lambda^*(\mathbf{r}) \cdot \frac{\partial^2\mathbf{P}(\mathbf{r}, t)}{\partial t^2}d\mathbf{r}. \tag{B8}$$

Obviously, via the expansion coefficients $\alpha_\lambda(t)$, the electric field $\mathbf{E}(\mathbf{r}, t)$ of Eq. (B3) is excited by the dipole source $\mathbf{P}(\mathbf{r}, t)$.

To simulate the two two-level quantum emitter, we adopt single-point dipole source $i = A, B$:

$$\mathbf{P}_i(\mathbf{r}, t) = D_i(t)\hat{\mathbf{d}}_i\delta(\mathbf{r} - \mathbf{r}_i) = \int_{-\infty}^{+\infty} d_i(\omega_i)e^{-i\omega_i t}d\omega_i\hat{\mathbf{d}}_i\delta(\mathbf{r} - \mathbf{r}_i). \tag{B9}$$

Here, $D_i(t)$ is the time-domain magnitude of the ith dipole source with, e.g., Gaussian profile, and $d_i(\omega_i)$ is its complex amplitude. $\hat{\mathbf{d}}_i$ and $\mathbf{r}_i$ are the direction and location of the ith dipole source, respectively. Substituting Eq. (B9) into Eq. (B8), we can obtain

$$\begin{aligned} \omega_\lambda^2&\alpha_\lambda(t) + \gamma\dot{\alpha}_\lambda(t) + \ddot{\alpha}_\lambda(t) \\ &= \frac{1}{\varepsilon_0}\int_{-\infty}^{+\infty} d_i(\omega_i)\omega_i^2 e^{-i\omega_i t}d\omega_i\mathbf{E}_\lambda^*(\mathbf{r}_i) \cdot \hat{\mathbf{d}}_i. \end{aligned} \tag{B10}$$

The solution of the linear Eq. (B10) is

$$\alpha_\lambda(t) = \frac{1}{\varepsilon_0}\int_{-\infty}^{+\infty} d_i(\omega_i)\frac{\omega_i^2}{\omega_\lambda^2 - i\gamma\omega_i - \omega_i^2}e^{-i\omega_i t}d\omega_i\mathbf{E}_\lambda^*(\mathbf{r}_i) \cdot \hat{\mathbf{d}}_i. \tag{B11}$$

Although the dissipation current density $\mathbf{J}_\gamma(\mathbf{r}, t)$ can be used to fix the precise position of the poles with respect to the integration contour in Eq. (B11), there is no need to calculate $\alpha_\lambda(t)$, by performing either frequency integration or contour integration via Eq. (B11). In fact, what really matters is the complex amplitude of $\alpha_\lambda(t)$ excited by the jth dipole source as

$$\alpha_{\lambda j}(\omega_j) = \frac{1}{\varepsilon_0}d_j(\omega_j)\frac{\omega_j^2}{\omega_\lambda^2 - i\gamma\omega_j - \omega_j^2}\mathbf{E}_\lambda^*(\mathbf{r}_j) \cdot \hat{\mathbf{d}}_j. \tag{B12}$$

Combining Eq. (B12) with Eq. (B3), we can obtain the complex amplitude of the electric field excited by the jth dipole source as

$$\mathbf{E}_j(\mathbf{r}, \omega_j) = \sum_\lambda \mathbf{E}_\lambda(\mathbf{r}) \frac{1}{\varepsilon_0} d_j(\omega_j) \frac{\omega_j^2}{\omega_\lambda^2 - i\gamma\omega_j - \omega_j^2} \mathbf{E}_\lambda^*(\mathbf{r}_j) \cdot \hat{\mathbf{d}}_j. \tag{B13}$$

Considering Eq. (B9), the complex amplitude of the current density corresponding to the ith dipole source is

$$\mathbf{J}_i(\mathbf{r}, \omega_i) = -d_i(\omega_i) i\omega_i \hat{\mathbf{d}}_i \delta(\mathbf{r} - \mathbf{r}_i). \tag{B14}$$

Similar to the time-averaged dipole emission power [78], we may adopt Eqs. (B13) and (B14) to define the complex dipole power:

$$\begin{aligned} R_{ij} &= -\frac{1}{2} \int_V d\mathbf{r} \mathbf{J}_i(\mathbf{r}, \omega_i) \cdot \mathbf{E}_j^*(\mathbf{r}, \omega_j) \\ &= -i \sum_\lambda \frac{d_i(\omega_i) d_j^*(\omega_j) \omega_i \omega_j}{4\varepsilon_0} [\hat{\mathbf{d}}_i \cdot \mathbf{E}_\lambda^*(\mathbf{r}_i)][\mathbf{E}_\lambda(\mathbf{r}_j) \cdot \hat{\mathbf{d}}_j] \\ &\quad \times \left[\mathcal{P} \frac{1}{\omega_j - \omega_\lambda} + i\pi\delta(\omega_j - \omega_\lambda) \right]. \end{aligned} \tag{B15}$$

Here, we assume $\omega_\lambda = \omega_j$, since the sum is dominated by the eigenmodes of the dielectric nanostructure whose eigenfrequencies ω_λ are close to the transition frequency of the quantum emitter ω_j. If we set ω_i as constant and ω_j as variable ω, then Eq. (B15) can be rewritten as

$$\begin{aligned} R_{i\omega} &= -\frac{1}{2} \int_V d\mathbf{r} \mathbf{J}_i(\mathbf{r}, \omega_i) \cdot \mathbf{E}_j^*(\mathbf{r}, \omega) \\ &= -i \sum_\lambda \frac{d_i(\omega_i) d_j^*(\omega) \omega_i \omega}{4\varepsilon_0} [\hat{\mathbf{d}}_i \cdot \mathbf{E}_\lambda^*(\mathbf{r}_i)][\mathbf{E}_\lambda(\mathbf{r}_j) \cdot \hat{\mathbf{d}}_j] \\ &\quad \times \left[\mathcal{P} \frac{1}{\omega - \omega_\lambda} + i\pi\delta(\omega - \omega_\lambda) \right]. \end{aligned} \tag{B16}$$

According to Eqs. (9) and (B16), we can obtain

$$W_{ij}^-(\omega) = -i \frac{u_i^* u_j}{\hbar d_i(\omega_i) d_j^*(\omega)\omega} \int_V d\mathbf{r} \mathbf{J}_i(\mathbf{r}, \omega_i) \cdot \mathbf{E}_j^*(\mathbf{r}, \omega). \tag{B17}$$

Here, we assume $\omega_\lambda = \omega_j$ once more. By substituting Eq. (B14) into Eq. (B17), we can further obtain Eq. (10).

[1] L. M. Duan, B. Wang, and H. J. Kimble, Phys. Rev. A **72**, 032333 (2005).

[2] M. Minkov and V. Savona, Phys. Rev. B **87**, 125306 (2013).

[3] M. Hensen, T. Heilpern, S. K. Gray, and W. Pfeiffer, ACS Photon. **5**, 240 (2017).

[4] H. J. Kimble, Nature **453**, 1023 (2008).

[5] A. O. Govorov, Phys. Rev. B **68**, 075315 (2003).

[6] A. O. Govorov, Phys. Rev. B **71**, 155323 (2005).

[7] G. Parascandolo and V. Savona, Phys. Rev. B **71**, 045335 (2005).

[8] E. V. Goldstein and P. Meystre, Phys. Rev. A **56**, 5135 (1997).

[9] S. Rist, J. Eschner, M. Hennrich, and G. Morigi, Phys. Rev. A **78**, 013808 (2008).

[10] P. Yao and S. Hughes, Opt. Express **17**, 11505 (2009).

[11] D. Dzsotjan, A. S. Sørensen, and M. Fleischhauer, Phys. Rev. B **82**, 075427 (2010).

[12] D. Martín-Cano, L. Martín-Moreno, F. J. García-Vidal, and E. Moreno, Nano Lett. **10**, 3129 (2010).

[13] D. Dzsotjan, J. Kästel, and M. Fleischhauer, Phys. Rev. B **84**, 075419 (2011).

[14] A. Gonzalez-Tudela, D. Martin-Cano, E. Moreno, L. Martin-Moreno, C. Tejedor, and F. J. Garcia-Vidal, Phys. Rev. Lett. **106**, 020501 (2011).

[15] K. J. Vahala, Nature **424**, 839 (2003).

[16] S. Reitzenstein *et al.*, Opt. Lett. **31**, 1738 (2006).

[17] A. Laucht *et al.*, Phys. Rev. B **82**, 075305 (2010).

[18] H. Kim, D. Sridharan, T. C. Shen, G. S. Solomon, and E. Waks, Opt. Express **19**, 2589 (2011).

[19] M. Calic, C. Jarlov, P. Gallo, B. Dwir, A. Rudra, and E. Kapon, Sci. Rep. **7**, 4100 (2017).

[20] F. Albert *et al.*, Nat. Commun. **4**, 1747 (2013).

[21] H. A. M. Leymann, A. Foerster, F. Jahnke, J. Wiersig, and C. Gies, Phys. Rev. Appl. **4**, 044018 (2015).

[22] F. Jahnke *et al.*, Nat. Commun. **7**, 11540 (2016).

[23] S. Lichtmannecker, M. Florian, T. Reichert, M. Blauth, M. Bichler, F. Jahnke, J. J. Finley, C. Gies, and M. Kaniber, Sci. Rep. **7**, 7420 (2017).

[24] J. P. Vasco, P. S. S. Guimarães, and D. Gerace, Phys. Rev. B **90**, 155436 (2014).

[25] B. Rigal, C. Jarlov, P. Gallo, B. Dwir, A. Rudra, M. Calic, and E. Kapon, Appl. Phys. Lett. **107**, 141103 (2015).

[26] J. P. Vasco, D. Gerace, P. S. S. Guimarães, and M. F. Santos, Phys. Rev. B **94**, 165302 (2016).

[27] R. H. Dicke, Phys. Rev. **93**, 99 (1954).

[28] M. Gross and S. Haroche, Phys. Rep. **93**, 301 (1982).

[29] B. M. Garraway, Philos. Trans. R. Soc. A **369**, 1137 (2011).

[30] B. Casabone, K. Friebe, B. Brandstätter, K. Schüppert, R. Blatt, and T. E. Northup, Phys. Rev. Lett. **114**, 023602 (2015).

[31] A. Neuzner, M. Körber, O. Morin, S. Ritter, and G. Rempe, Nat. Photon. **10**, 303 (2016).

[32] M. O. Pleinert, J. von Zanthier, and G. S. Agarwal, Phys. Rev. A **97**, 023831 (2018).

[33] M.-O. Pleinert, J. von Zanthier, and G. S. Agarwal, Optica **4**, 779 (2017).

[34] J. Xu, S. Chang, Y. Yang, S. Zhu, and G. S. Agarwal, Phys. Rev. A **96**, 013839 (2017).

[35] F. W. Cummings and A. Dorri, Phys. Rev. A **28**, 2282 (1983).

[36] A. A. Zhukov, D. S. Shapiro, W. V. Pogosov, and Y. E. Lozovik, Phys. Rev. A **96**, 033804 (2017).

[37] S. V. Remizov, A. A. Zhukov, W. V. Pogosov, and Y. E. Lozovik, Laser Phys. Lett. **16**, 065205 (2019).

[38] T. Kobayashi, Q. Zheng, and T. Sekiguchi, Phys. Rev. A **52**, 2835 (1995).

[39] M. Wubs, L. G. Suttorp, and A. Lagendijk, Phys. Rev. A **70**, 053823 (2004).

[40] S. Hughes, Phys. Rev. Lett. **94**, 227402 (2005).

[41] Y.-G. Huang, G. Chen, C.-J. Jin, W. M. Liu, and X.-H. Wang, Phys. Rev. A **85**, 053827 (2012).

[42] A. Taflove and S. C. Hagness, *Computational Electrodynamics: The Finite-Difference Time-Domain Method*, 3rd ed. (Artech House, Boston, 2005).

[43] Z. Ficek and S. Swain, *Quantum Interference and Coherence: Theory and Experiments* (Springer, New York, 2005), p. 70.

[44] Y. Akahane, T. Asano, B.-S. Song, and S. Noda, Nature **425**, 944 (2003).

[45] X.-H. Wang, R. Wang, B.-Y. Gu, and G.-Z. Yang, Phys. Rev. Lett. **88**, 093902 (2002).

[46] X.-H. Wang, B.-Y. Gu, R. Wang, and H.-Q. Xu, Phys. Rev. Lett. **91**, 113904 (2003).

[47] C. Cohen-Tannoudji, J. Dupont-Roc, and G. Grynberg, *Atom-photon Interactions: Basic Processes and Applications* (John Wiley & Sons, New York, 1992), p. 170.

[48] G. Chen, Y.-C. Yu, X.-L. Zhuo, Y.-G. Huang, H. Jiang, J.-F. Liu, C.-J. Jin, and X.-H. Wang, Phys. Rev. B **87**, 195138 (2013).

[49] Y. Zhang, W. Zheng, M. Xing, G. Ren, H. Wang, and L. Chen, Opt. Commun. **281**, 2774 (2008).

[50] C. Sauvan, J. P. Hugonin, I. S. Maksymov, and P. Lalanne, Phys. Rev. Lett. **110**, 237401 (2013).

[51] D. S. Dovzhenko, S. V. Ryabchuk, Y. P. Rakovich, and I. R. Nabiev, Nanoscale **10**, 3589 (2018).

[52] D. Hofmann, T. Körzdörfer, and S. Kümmel, Phys. Rev. A **82**, 012509 (2010).

[53] A. R. A. Chalcraft *et al.*, Appl. Phys. Lett. **90**, 241117 (2007).

[54] G. Chen, J.-F. Liu, H. Jiang, X.-L. Zhuo, Y.-C. Yu, C. Jin, and X.-H. Wang, Nanoscale Res. Lett. **8**, 187 (2013).

[55] P. Lodahl, S. Mahmoodian, and S. Stobbe, Rev. Mod. Phys. **87**, 347 (2015).

[56] G. Chen, J.-F. Liu, H.-X. Jiang, G. Liu, Y. Chen, Z. Chen, and X.-H. Wang, J. Phys. B: At. Mol. Opt. Phys. **52**, 035503 (2019).

[57] J. D. Joannopoulos, S. G. Johnson, J. N. Winn, and R. D. Meade, *Photonic Crystals: Molding the Flow of Light*, 2nd ed. (Princeton University Press, Princeton and Oxford, 2008), p. 147.

[58] P. T. Kristensen, C. Van Vlack, and S. Hughes, Opt. Lett. **37**, 1649 (2012).

[59] S. A. Crooker, J. A. Hollingsworth, S. Tretiak, and V. I. Klimov, Phys. Rev. Lett. **89**, 186802 (2002).

[60] G. Chen, J.-F. Liu, Y.-C. Yu, R. Liu, G. Zhu, Y. Chen, Z. Chen, and X.-H. Wang, Sci. China: Phys. Mech. Astron. **62**, 64211 (2019).

[61] T. Yoshie, A. Scherer, J. Hendrickson, G. Khitrova, H. M. Gibbs, G. Rupper, C. Ell, O. B. Shchekin, and D. G. Deppe, Nature **432**, 200 (2004).

[62] D. Englund, A. Faraon, I. Fushman, N. Stoltz, P. Petroff, and J. Vuckovic, Nature **450**, 857 (2007).

[63] A. Faraon, I. Fushman, D. Englund, N. Stoltz, P. Petroff, and J. Vuckovic, Nat. Phys. **4**, 859 (2008).

[64] M. Nomura, N. Kumagai, S. Iwamoto, Y. Ota, and Y. Arakawa, Nat. Phys. **6**, 279 (2010).

[65] J. Q. Grim *et al.*, Nat. Mater. **18**, 963 (2019).

[66] K. Hennessy, A. Badolato, M. Winger, D. Gerace, M. Atature, S. Gulde, S. Falt, E. L. Hu, and A. Imamoglu, Nature **445**, 896 (2007).

[67] A. Badolato, K. Hennessy, M. Atatüre, J. Dreiser, E. Hu, P. M. Petroff, and A. Imamoğlu, Science **308**, 1158 (2005).

[68] P. T. Kristensen, J. Mørk, P. Lodahl, and S. Hughes, Phys. Rev. B **83**, 075305 (2011).

[69] H. Takagi, Y. Ota, N. Kumagai, S. Ishida, S. Iwamoto, and Y. Arakawa, Opt. Express **20**, 28292 (2012).

[70] H. Choi, M. Heuck, and D. Englund, Phys. Rev. Lett. **118**, 223605 (2017).

[71] S. Hu, M. Khater, R. Salas-Montiel, E. Kratschmer, S. Engelmann, W. M. J. Green, and S. M. Weiss, Sci. Adv. **4**, eaat2355 (2018).

[72] H. Choi, D. Zhu, Y. Yoon, and D. Englund, Phys. Rev. Lett. **122**, 183602 (2019).

[73] R. Liu, Z.-K. Zhou, Y.-C. Yu, T. Zhang, H. Wang, G. Liu, Y. Wei, H. Chen, and X.-H. Wang, Phys. Rev. Lett. **118**, 237401 (2017).

[74] H. Leng, B. Szychowski, M.-C. Daniel, and M. Pelton, Nat. Commun. **9**, 4012 (2018).

[75] Y.-W. Lu, L.-Y. Li, and J.-F. Liu, Sci. Rep. **8**, 7115 (2018).

[76] Z.-K. Zhou, J. Liu, Y. Bao, L. Wu, C. E. Png, X.-H. Wang, and C.-W. Qiu, Prog. Quantum Electron. **65**, 1 (2019).

[77] Y. Xu, J. S. Vučković, R. K. Lee, O. J. Painter, A. Scherer, and A. Yariv, J. Opt. Soc. Am. B **16**, 465 (1999).

[78] J. D. Jackson, *Classical Electrodynamics*, 3rd ed. (Wiley, New York, 1999), p. 265.